XFEL coherent diffraction imaging for weakly scattering particles using heterodyne interference

Cite as: AIP Advances **10**, 055219 (2020); https://doi.org/10.1063/1.5129406
Submitted: 04 February 2020 • Accepted: 07 April 2020 • Published Online: 20 May 2020

Chi-Feng Huang, Wei-Hau Chang, Ting-Kuo Lee, et al.

XFEL coherent diffraction imaging for weakly scattering particles using heterodyne interference

Cite as: AIP Advances 10, 055219 (2020); doi: 10.1063/1.5129406
Submitted: 4 February 2020 • Accepted: 7 April 2020 •
Published Online: 20 May 2020

Chi-Feng Huang,[1] Wei-Hau Chang,[1,2,a)] Ting-Kuo Lee,[1,b)] Yasumasa Joti,[3] Yoshinori Nishino,[4] Takashi Kimura,[4] Akihiro Suzuki,[4] Yoshitaka Bessho,[1] Tsung-Tse Lee,[1] Mei-Chun Chen,[1] Shun-Min Yang,[1] Yeukuang Hwu,[1] Shih-Hsin Huang,[2] Po-Nan Li,[1,c)] Peilin Chen,[5] Yung-Chieh Tseng,[6] Che Ma,[6] Tsui-Ling Hsu,[6] Chi-Huey Wong,[6] Kensuke Tono,[7] Tetsuya Ishikawa,[7] and Keng S. Liang[1]

AFFILIATIONS

[1]Institute of Physics, Academia Sinica, Taipei 115, Taiwan
[2]Institute of Chemistry, Academia Sinica, Taipei 115, Taiwan
[3]Japan Synchrotron Radiation Research Institute/Spring-8, Hyogo 679-5198, Japan
[4]Research Institute for Electronic Science, Hokkaido University, Sapporo 001-0021, Japan
[5]Research Center for Applied Sciences, Academia Sinica, Taipei 115, Taiwan
[6]Genomics Research Center, Academia Sinica, Taipei 115, Taiwan
[7]RIKEN SPring-8 Center, Hyogo 679-5148, Japan

[a)]**Author to whom correspondence should be addressed:** weihau@chem.sinica.edu.tw
[b)]**Current address:** Department of Physics, National Sun Yat-sen University, Kaohsiung 80424, Taiwan.
[c)]**Current address:** Department of Electrical Engineering, Stanford University, Stanford, CA 94305, USA.

ABSTRACT

The spatial resolution of x-ray free-electron laser (XFEL) coherent diffraction imaging is currently limited by the fluence of XFELs. Here, we clarify this issue by systematically studying the diffraction with a SPring-8 angstrom compact free electron laser XFEL on gold nanoparticles of size from 10 nm to 80 nm in water solution. The coherent x-ray diffraction patterns obtained from single XFEL pulses were quantitatively analyzed using a small-angle x-ray scattering scheme along with computer simulations. The results show that the detectability of Au nanoparticles can be described by a "master curve" as a function of total electron density, particle size, and x-ray fluence. The difficulty in detecting a small particle under the current XFEL fluence, however, could be largely eliminated by the image enhancement effect through interference from a strong scattering nanoparticle nearby. We investigate this image enhancement effect by quantitatively analyzing the two-particle scattering from Au nanoparticles, and further, applying it to detect a weak biological object of influenza virus with the aid of an Au nanoparticle.

I. INTRODUCTION

In the wake of the inauguration of the first two x-ray free-electron laser (XFEL) facilities, the Linac Coherent Light Source (LCLS) at SLAC in 2009[1] and the SPring-8 Angstrom Compact free electron laser (SACLA) at SPring-8 in 2012,[2] intense interests have emerged to explore the structure and dynamics of both material and biological systems with the employment of unprecedented brilliant femtosecond x-ray pulses. The highly coherent nature of XFEL beams has promised the lens-less x-ray imaging technique, the coherent x-ray diffraction imaging (CXDI), to achieve, in principle, an image resolution of the wavelength of x-ray photons, which is particularly attractive for the study of complex and disordered systems.[3–5] In addition, the ultra-short x-ray pulses of the XFEL enable a "diffraction before damage" strategy[6–8] to allow for CXDI to access radiation-sensitive specimens, such as living cells[9] and active catalyst structures.[10]

It is well known that in current XFELs, the beam fluence is still insufficient, in particular, for biomolecules <10 nm[11] to scatter enough photons at a high angle required for high-resolution

image reconstruction.[12] To circumvent the limitations imposed by the beam fluence, a number of reports have addressed the ways of enhancing signals by exploiting the coherent nature of the x-ray sources.[13–18] However, a quantitative understanding of how the beam fluence would limit the scattering has remained unclear.

In this report, we systematically investigate the intensity issues of coherent x-ray diffraction (CXD) by performing in-solution one-particle scattering of Au nanoparticles (AuNPs) of sizes ranging from a few nanometers up to ~80 nm, recovering the missing central intensities by iterative phase-retrieval technique, and analyzing them with the framework of conventional small-angle x-ray scattering (SAXS) with validation by computer simulations. By plotting the scattering intensity at zero momentum transfer extrapolated from the experimental data of AuNPs of different sizes, a master curve was established. This curve compares well with the ideal one calculated from AuNPs of known electron densities and where the curve vanishes defines the particle detectability, explaining that the current XFEL fluence at SACLA (10^{12} μm^{-2}) and those at all other facilities with similar fluence, is insufficient to allow the detection of <10 nm particles.

Since the ultimate goal of this line of investigation is to develop a photonics strategy to detect the weak scatters of biological objects, we explore the possibility of enhancing the detection of smaller scatters that are excluded by the "master curve" using the heterodyne interference effect. To this end, we first quantify the image enhancement effect in the Young's interference patterns generated from two-particle scattering[16] under our experimental conditions. Our experimental results demonstrate that the enhancement effect conferred by a 40 nm AuNP can reveal an otherwise invisible single particle of 20 nm AuNP nearby. Next, we applied this technique to a specimen of a mixture of AuNP (40 nm) and influenza virus (100 nm). It is noted that the influenza virus is a two-component system that has an electron-dense genome encapsulated by a protein coat. Notably, plausible densities accommodating the genome materials stood out in the reconstructed image, demonstrating this enhancement effect as a provisional remedy for imaging weakly scattering biological objects in solution before the eventual increase in the XFEL fluence.

II. EXPERIMENTAL SETUP AND ANALYTIC METHODS

The CXDI measurements were performed in six separate runs during a three-year period at beamline 3 (BL3) of SACLA[19] with a photon energy set at 4 keV (6.4×10^{-16} J/photon or 3.1 Å) and a pulse duration of ~10 fs.[20] The pulse energy (in micro Joule) varied in each run and fluctuated in a range of standard deviation (SD) from 6% to 12% [see Fig. 1(a)]. At BL3, a pair of Kirkpatrick–Baez mirrors focus the beam at the sample position to a spot of a full width at half maximum (FWHM) ~1.5 μm[20] to achieve a fluence of ~10^{12} photons/μm^2, higher than the nominal annual fluence at SACLA (1.6×10^{14} photons/mm^2).[21] For a single nanoparticle with a known electron density (e.g., gold), the size of the particle and the location of the particle in the x-ray beam can be inferred from SAXS intensity analysis, as discussed below in detail. Single-shot CXD patterns were recorded with a multi-port charge-coupled

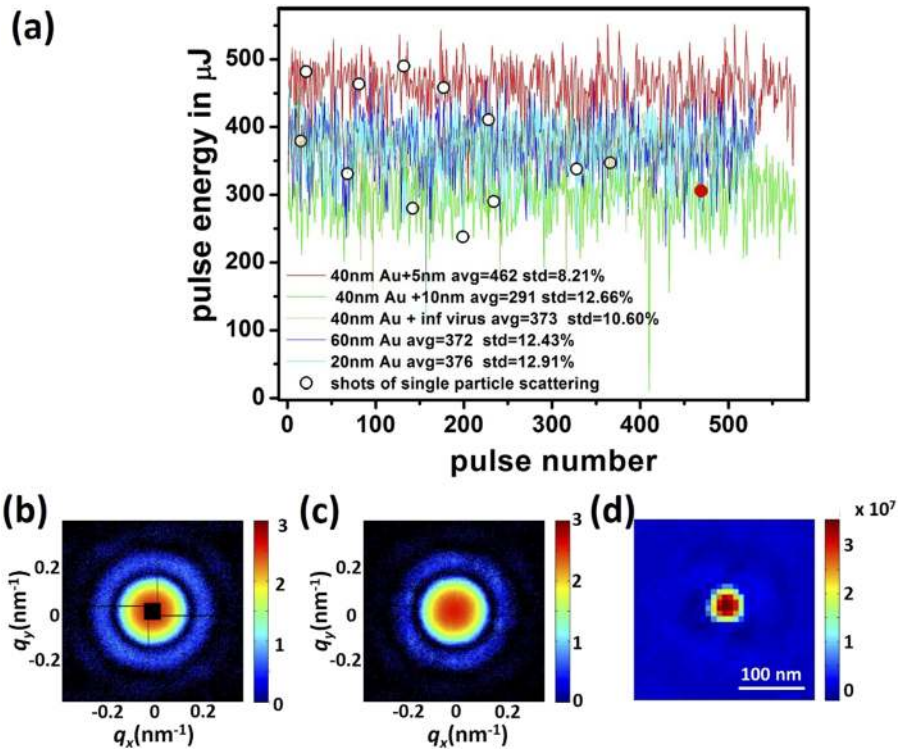

FIG. 1. XFEL pulse variations, the CDX diffraction pattern, and the reconstructed image. (a) The variations of the XFEL pulse energy at the exit of the undulator recorded in each experimental run. The shots for single AuNP scattering that present data in the text are marked with open circles (◯). (b) The XFEL-CXD pattern of a 60 nm AuNP from a shot [red filled circle in Fig. 1(a)]. The central region that is missing due to the beam stop is computationally masked. (d) The reconstructed image by phase-retrieval from (b). (c) Back transformed pattern of (d), where the central region is now filled. The scale of the color bar in the diffraction pattern is the logarithm of photon counts and in the phase-retrieved image is linear (a.u.).

device (MPCCD)[21] detector (2048 × 2048 pixels^2) with a pixel size of 50 μm. In our experiments, the detector was located at 1.51 m from the sample.[21] At such a detector distance, the edge of the MPCCD corresponds to a cutoff scattering vector q = 0.7 nm^{-1}, where $q = (4\pi \sin\theta/\lambda)$ with λ, the wavelength and 2θ, the scattering angle. For the particle size of 40–60 nm of AuNPs, the detector can cover a q range in the flat Guinier region to accommodate several intensity oscillations in the SAXS curve so that the quantitative data analysis can be performed.[22] These experimental parameters also determine the ceiling of image resolution of the CXD measurements.

The AuNPs were chosen for our model study because one of the main parameters in the SAXS analysis, the electron density of the sample (gold, ρ_{Au}), is known. The AuNPs employed in the study have particle sizes, as taken from the labels of the supplier (BBI Solutions, UK), of 10 nm, 20 nm, 40 nm, 60 nm, and 80 nm. All samples used in the experiments were subjected to the cryo-electron microscopy examination before the x-ray measurements. The nanoparticles were prepared in water solution sealed in micro-liquid enclosure, as in the previous pulsed coherent x-ray solution scattering (PCXSS) method.[9] In brief, the solution sample is loaded in a micro-liquid enclosure array (MLEA) chip.[9] One MLEA chip contains 24 × 24 independent micro-liquid enclosures separated by partitions and holds the solution sample in between two thin SiN membranes with a solution layer thickness of 2 μm.[9] Since the elastic mean free path of 4 keV x ray for water is 1.4 cm, ~10^4 times of the water column here, it is reasonable to assume that the elastic scattering occurs at most, either by the sample or by the water molecule. Each liquid enclosure has an x-ray illuminating window of 20 × 20 μm^2 in size and the window frame acts as a guard slit in the sample plane to reduce parasitic scattering from upstream optics. The MLEA chips were mounted in the multiple application x-ray imaging chamber (MAXIC) that was kept in a vacuum of ~10^{-3} Pa.[23] For each sample, the particle concentration in the liquid solution was adjusted to maximize the probability of only one particle to be intercepted by the XFEL beam. In our measurements, the hitting rate, i.e., the probability of the 1.5 μm beam to hit some nanoparticles, was found to be about 5%–10% that is comparable to those in aerosol injector systems commonly used in CXDI experiments.[24] Among thousands of diffraction patterns collected, we first grouped the diffraction patterns into different symmetric features, from which the patterns with a simple concentric signature were selected for SAXS analysis [Fig. 1(b)]. Such "good" patterns count about 1% of the total patterns collected. Many coherent x-ray diffraction (CXD) patterns containing multi-particle scattering are excluded from further analysis for this report.

The scattered intensity $I_{sc}(\mathbf{q})$ recorded by the MPCCD detector element subtending a solid angle $\Delta\Omega$ can be expressed as[25,26]

$$I_{sc}(\mathbf{q}) = \Delta\Omega I_0 (r_e)^2 |F(\mathbf{q})|^2, \tag{1}$$

where I_0 is the incident x-ray intensity of the specific pulse [as marked in Fig. 1(a) for the corresponding CXD pattern], r_e is the classical electron radius (2.8 × 10^{-15} m), and $\Delta\Omega$ is the solid angle that is estimated to be 1.1 × 10^{-9}. $|F(\mathbf{q})|$ is the absolute value of the form factor, as determined from the measured CXD pattern. It is noted that the quantum efficiency of the MPCCD at 4 keV is about 99%.[21] When a finite object is illuminated by a coherent x-ray beam and its far-field diffracted waves fulfill the Born approximation, the form factor $F(\mathbf{q})$ is the Fourier transform of electron density $\rho(\mathbf{r})$:[26]

$$\mathrm{F}(\mathbf{q}) = \int_{\infty}^{-\infty} \rho(\mathbf{r}) e^{-i\mathbf{q}\cdot\mathbf{r}} d\mathbf{r}. \tag{2}$$

Since the anomalous scattering and Ewald sphere curvature can be neglected for the present study, we assumed the validity of the phase the object holds,[27] and thereby, centro-symmetrized the measured diffraction patterns,[28–30] and 4 × 4 binned them to improve the signal-to-noise ratio (S/N). Practically, sometimes the intensity in the fourth quadrant is blocked by a beam stop due to the experimental setting, and the resultant missing diffraction would hamper the reconstruction of the real space image, for which centro-symmetrization can be used for mitigation. A home-built program which combines the guided hybrid input–output (GHIO)[31] algorithm and the shrink-wrap (SW)[32] algorithm was employed to retrieve the phase from the diffraction pattern to reconstruct the image. The reconstruction started with an initial support derived from the inverse Fourier transform of the measured intensity. At the end of each generation of the reconstruction, the copy with the lowest Fourier-domain error E_F is selected, with E_F as

$$E_F = \frac{\sum_q ||\mathrm{F(q)}| - |\mathrm{K(q)}||}{\sum_q |\mathrm{F(q)}|}, \tag{3}$$

in which $\mathrm{K}(\mathbf{q})$ is the Fourier transform of the reconstructed electron density $\rho(\mathbf{r})$. In $|K(\mathbf{q})|$, the missing information in the central region is restored.

Figure 1(b) shows a typical pattern from a single spherical 60 nm AuNP. For a good set of data, the GHIO analysis usually converges at the tenth generation of iteration to an error factor E_F 0.18 based on comparing the background corrected pattern [e.g., Fig. 1(b)] and the back-transformed pattern [e.g., Fig. 1(d)]. For the AuNPs with sizes less than 80 nm, the intensity data collected by the MPCCD detector at 1.51 m is sufficient for such analysis. We note that the measured intensity data in our experiment falling below the noise level for $q > 0.5$ nm^{-1} in spite that gold is a very strong scatterer.

The experimental SAXS intensity curve, which is of one dimension, is obtained from circularly averaging the two-dimension diffraction intensities at given radial scattering momentum transfer denoted by vector q. The CXD patterns of spherical particles are then subjected to detailed SAXS intensity analysis to determine the "goodness" of the data. A good data should show a flat curve at the low q region and some intensity dips at high q. As an example, the SAXS curve is shown as a black open circle in Fig. 2, which is obtained from Fig. 1(c). The experimental SAXS curve is compared with a simulation based on a spherical hard-wall model[33]

$$I_{sphere}(\mathrm{q}, R_{\mathrm{Au}}) = [F_{\mathrm{Au}}(0)]^2 [3\frac{\sin(qR_{\mathrm{Au}}) - (qR_{\mathrm{Au}})\cos(qR_{\mathrm{Au}})}{(qR_{\mathrm{Au}})^3}]^2, \tag{4}$$

$$F_{\mathrm{Au}}(0) = \frac{4}{3}\pi (R_{\mathrm{Au}})^3 \rho_{\mathrm{Au}} = V_{\mathrm{Au}}\rho_{\mathrm{Au}}, \tag{5}$$

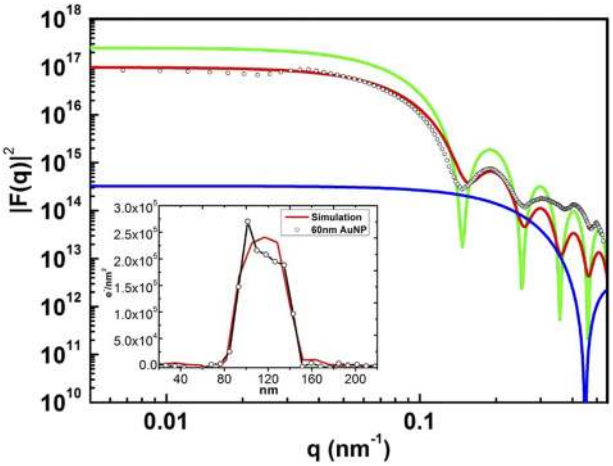

FIG. 2. The SAXS intensity curves of AuNP: open circle represents experimental points; red solid line represents the fitted curve with Gaussian σ = 0.015; green solid line represents a simulated curve of a spherical AuNP particle of the diameter 61 nm that matches the nodes in the experiment points; and blue solid line is a simulated curve of a 20 nm AuNP. Note that the experimental curve of a 20 nm AuNP is not available. The inset is the simulated electron density profile in comparison with the profile retrieved from measurement as in Fig. 1(c).

where R_{Au} is the radius and V_{Au} is the volume of AuNP. To model an ideal master curve of AuNPs, the electron density of the fcc Au crystal (4633 e^-/nm^3) is applied to ρ_{Au}.

By matching the oscillations on a curve calculated from a model of spherical hard-wall using Eq. (4) (e.g., green curve in Fig. 2) with the nodes in the measured intensities, the radius of an Au particle can be determined. With the assumption of a spherical shape, the volume of the sample can be estimated. To further render the calculated SAXS intensity comparable with the experimental one, Gaussian smearing (σ) using Eqs. (6) and (7) below is performed using a kernel[34] that takes account of the blurring by instrumentation factors,

$$I_{Gs}(q) = \int_{q'} g(q - q', \sigma) I_{sphere}(q) dq', \tag{6}$$

$$g(q, \sigma) = \frac{1}{\sqrt{2\pi\sigma}} \exp[-\frac{q^2}{2\sigma}]. \tag{7}$$

Finally, the calculated curve is shifted to the lower intensity to match the measurement in the flat Guinier region to take into account the effect of the particle location relative to the beam center.

It can be readily seen from Eqs. (1) and (5) that the scattering intensity at zero momentum transfer is proportional to the x-ray fluence on the sample and the square of the total electron density of the particle, i.e.,

$$I_{sc}(0) = \Delta\Omega I_0 (r_e)^2 [V_{\mathrm{Au}} \rho_{\mathrm{Au}}]^2. \tag{8}$$

However, it should be noted that when the medium effect cannot be neglected, the density should be replaced by the difference in densities between the particle and the medium. The scattering intensities from a hydrated protein would become[35–37]

$$I_{sc}(0) = \Delta\Omega I_0 (r_e)^2 (V_{\mathrm{Au}})^2 (\rho_{prot} - \rho_{sol} u)^2, \tag{9}$$

where ρ_{prot} is the number of electrons per mass of dry protein and ρ_{sol} is the density of electrons of water, and u is the partial specific volume of protein. These values are 3.22 × 10^{23} e^-/g, 3.34 × 10^{23} e^-/cm^3, and 0.73 cm^3/g, respectively.[35]

III. RECOVERY OF MISSING *F*(0) FROM THE DIFFRACTION PATTERN

To perform the Giunier analysis required for a SAXS scheme, it is important to use the low q information. Unfortunately, these data are missing from the diffraction pattern because the central region is masked due to the beam stop [e.g., Fig. 1(b)]. To recover those missing data, we first subtracted the background from the diffraction pattern, and then, retrieved the phases for the pattern [Fig. 1(b)] using GHIO[31] to obtain a reconstructed image [Fig. 1(d)]. By back-transforming the image, a new pattern was obtained, in which the information at low q was restored [Fig. 1(c)]. Circularly averaging the new 2D diffraction pattern produces a 1D SAXS curve (see Fig. 2). As the scattering intensities depend on the fluence that varies from shot to shot, we normalized the intensity based on Eq. (1) to make the comparison on the same ground. The obtained $[F(0)]^2$ represents the effective scattering intensities free from the instrumentation parameter, such as the beam fluence. It can be readily seen from Eq. (5) that the $F(0)$ reflects the total number of electrons of a sample in the ideal case. When the $F(0)$ is determined from the experimental data, we endow it to the total number of "effective" electrons.

IV. SAXS ANALYSIS AND MASTER CURVE

Figure 2 shows an experimental SAXS curve (red line) fitted to the measurements (empty circles) from an AuNP particle from the batch of 60 nm. This curve agrees well with a calculated SAXS curve (green line) using a model of 61 nm AuNP sphere at the oscillation for $q < 0.23\ \mathrm{nm}^{-1}$. Furthermore, the electron density profile in the image reconstructed from the measured pattern agrees with that from the simulation of an ideal sphere model (see the inset of Fig. 2). By integrating the total charges in the 2D density map (see the inset of Fig. 2) and dividing it over the volume of a 61 nm sphere, we obtained 4310 e^-/nm^3, the effective total electron density of the Au particle. Remarkably, this value agrees well with that of fcc Au (4633 e^-/nm^3). However, the experimental curve evidently deviates from that of a sphere for $q > 0.23\ \mathrm{nm}^{-1}$, which indicates that the actual particle is not an ideal sphere. In fact, different shapes of particles from the same batch of AuNPs were observed by cryo-EM prior to the XFEL CDX experiment, including rounded fcc nanocrystals, ellipsoidal, and spherical particles (data not shown). Nonetheless, the deviation in the SAXS curve at a high q does not affect the estimation of $F(0)$, the total number of electrons.

All the shots that give "good" spherical patterns of AuNPs, as marked in Fig. 1, are selected and similarly analyzed. The average standard deviation of pulse energy of these good shots is 11.55%. Assuming that the beamline optics delivered a photon flux at the

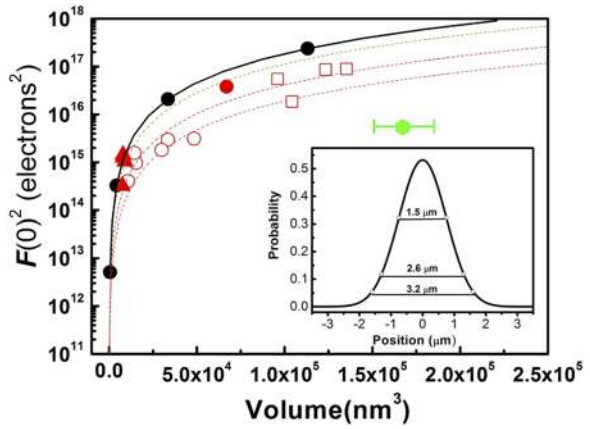

FIG. 3. The master curve of "normalized" scattering intensity $F(0)^2$ vs AuNP particle size (volume). The solid black curve is the simulated scattering intensity based on a hard sphere placed at the beam center; the black filled circles are the calculated scattering intensity of 10 nm, 20 nm, 40 nm, and 60 nm AuNPs, respectively, where the dotted curves denote the simulated scattering intensity when the sample is away from the beam center, by 0.75 (gray), 1.3 (red), and 1.6 μm (pink), respectively. Green filled circle represents the simulated intensity from the capsid of a Rift Valley fever virus particle of 100 nm. The experimental data shown are red open circle, single 40 nm AuNP; red open square, single 60 nm AuNP; red filled circle, twin 40 nm AuNPs; and red filled triangle, twin 20 nm AuNPs. The inset is the intensity profile of a Gaussian beam with a FWHM of 1.5 μm.

sample position in a consistent way from the source, the intensity data collected in different pulses can then be normalized using the measured pulse energy. Figure 3 summarizes the experimental scattering intensities $[F(0)]^2$ from all "good" data obtained from spherical AuNPs together with a theoretical $[F(0)]^2$ curve (black line) calculated using Eq. (5). In Fig. 3, we observe that the scattering intensities from AuNPs of a given size are well clustered but deviate from the theoretical curve. We have noticed this discrepancy in individual SAXS curves. As shown in Fig. 2 (e.g., the green curve), there is a sizable gap between the measured intensity and the calculated curve in the flat Guinier region (low q). This mismatch cannot be quantitatively explained by the detector performance or the sample system since the detector quantum efficiency at the wavelength used here (3.1 Å) is close to 100% and the attenuation by a 2 μm water column is insignificant. Instead, this deviation can be largely accounted for by modeling the particle location away from the peak position of the beam with a profile with a Gaussian with a FWHM ~ 1.5 μm (inset of Fig. 3).

V. AuNP PARTICLE SIZE ANALYSIS AND THE LIMIT IN XFEL SINGLE PARTICLE IMAGING

The beam profile effects can also explain the low probability of obtaining "good" data since the chances of a single spherical AuNP situated inside the 1.5 μm zone of the x-ray beam are rare. The results shown in Fig. 3 allow us to assess the limit in imaging AuNPs by CXDI. Experimentally, faint speckle signals from a 20 nm AuNP can be observed in the flat Guinier region (low q) but attempts to reconstruct the image were unsuccessful due to photon-limited data at a high q. We found the scattering of a 20 nm AuNP above $q = 0.3$ nm^{-1} is below ten photon counts in the 4 × 4 binned data. The low quality speckle signals in the low q together with the signal cutoff at the high q conferred by a 20 nm AuNP suggest that the detection limit of CDXI imaging at this beamline is set. As the detector performance and the reconstruction algorithms are not the limiting factors, we conclude the detection limit is largely dependent on the fluence.

Although a single 20 nm AuNP could not provide the $[F(0)]^2$ due to the failure of convergence in image reconstruction, the strip patterns of two 20 nm AuNPs (a twin particle) in the Guinier region could be observed in several samples, from which $[F(0)]^2$ could be extracted. The obtained values of such twin particles also follow the master curve nicely (triangle data points in Fig. 3). The $[F(0)]^2$ measurements were then similarly obtained from a twin 40 nm particle, also presented in Fig. 3 for comparison. The ability to reconstruct twin 20 nm particles but not a single 20 nm particle is due to the heterodyne amplification effect that raises S/N in the high q region.[16] With the beamline BL3 at SACLA that delivers 4.0 keV x-ray photons (3.1 Å) with a flux on the order of ~10^{12} [photons/(μm^2/pulse)], which is achieved with the aid of the KB mirror for focusing to a beam size of 1.5 μm, our results suggest that achieving the CXDI of a smaller particle, say 5 nm AuNP, entails an increase of the fluence by at least three orders of magnitude.

VI. ENHANCING VISIBILITY OF WEAK SCATTER USING HETERODYNE INTERFERENCE

The merit of taking the diffraction image by CXDI is that the phase information encoded in scattered photons is recorded. If there are two particles in the field, they can be identified given the resulting CXD pattern has a stripe feature. Following the heterodyne holography principle described by Shintake,[16] the phase information of both scatters can be retrieved, for which we employed the GHIO algorithm[31] in analyzing the two-dimensional stripe patterns in this study. The two particles are assumed to be in the same plane normal to the beam in the analysis.[38,39]

Based on the master curve, the 40 nm AuNP can be readily detected as a single particle. We, thereby, chose 40 nm AuNP as a reference scatterer[16] and explored the possibility of obtaining experimental interference patterns between a 40 nm AuNP and a smaller AuNP, for which we mixed 40 nm AuNPs with 20 nm, 10 nm, and 5 nm AuNPs, respectively, in this study. Experimental CXDI patterns from the mixture of 40–10 nm and 40–5 nm gave poor S/N such that the GHIO analysis failed to yield meaningful results. As shown in Fig. 4(a), the strip patterns from twin 40–20 nm AuNPs provided a clear interference signature with a good SNR to allow for image reconstruction [Fig. 4(b)]. The identity of this 20 nm AuNP is validated by the simulations shown in Figs. 4(c) and 4(d), and is further supported by good agreement between the measured electron density profile and that of simulation [Fig. 4(e)]. In Fig. 4(e), we also documented the simulation results of AuNPs of various sizes enhanced by the 40 nm AuNP. Notably, the total number of electrons of the particle estimated from the reconstructed density profiles of 40 nm, 20 nm, and 10 nm are 6.7 × 10^7, 7.3 × 10^6, and 7.5 × 10^5, respectively. These values represent 45%, 39%, and 32% of the anticipated figures, indicating that the enhancement effect only partially

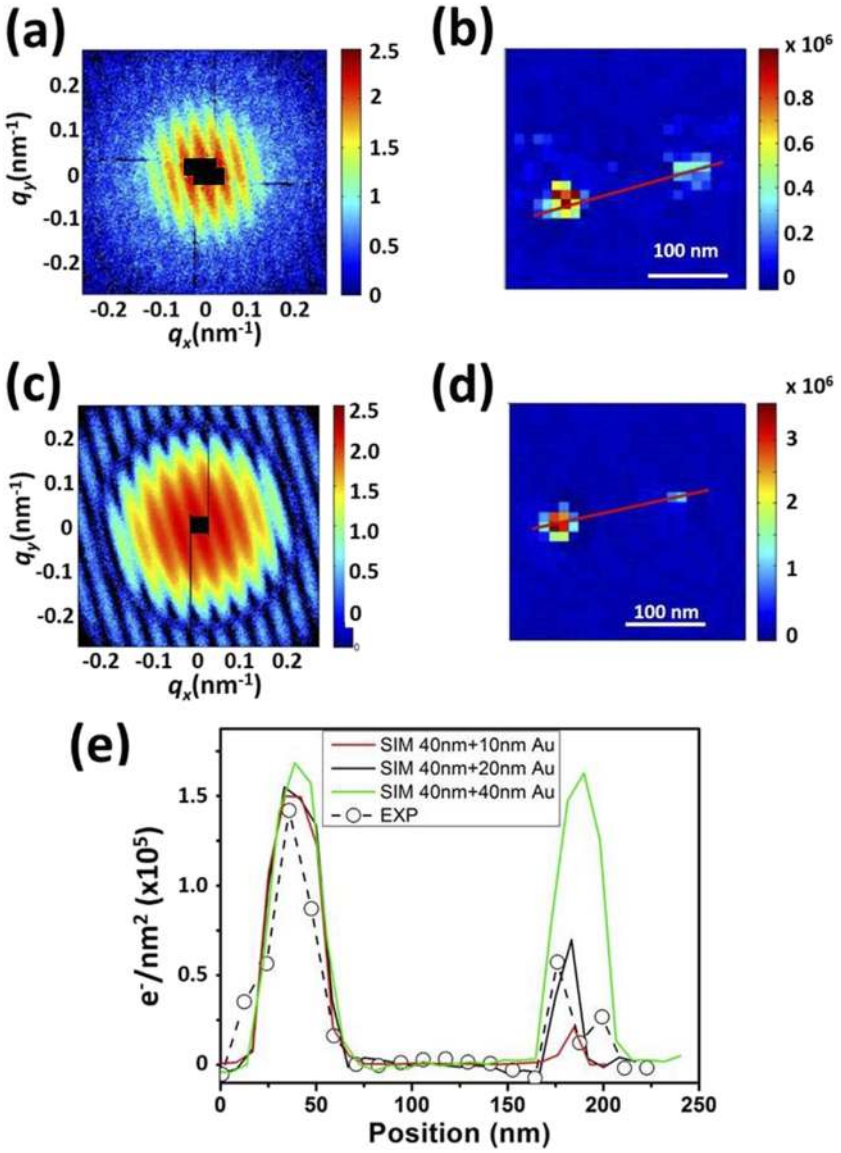

FIG. 4. Two AuNPs interference. (a) An experimental interference pattern from a strong scatter (40 nm AuNP) with a weak scatter (20 nm AuNP). Note that the missing central region is further computationally masked. (b) The reconstructed image of (a). (c) The simulated interference pattern from a 40 nm AuNP with a 20 nm AuNP that is placed 135 nm away to simulate the experimental interference. (d) The reconstructed image of (c). (e) The electron density profiles of the experimental image (◯) vs simulated images (—) along the red line in (b) and (d). The scale of the color bar is logarithmic in the diffraction pattern and linear in the reconstructed image (a.u.).

recovers the signals of the target. It appears that the smaller the target, the less the efficiency of recovery. This simulation study also suggests that the two-particle enhancement scheme is able to extend the detection limit of the current SACLA XFEL to an AuNP of 10 nm, but perhaps not beyond.

VII. BIOLOGICAL APPLICATION

To explore if this fluence at a SACLA beamline can be extended to weakly scatters, we targeted an influenza virus of ~100 nm size[40] since the early XFEL study with a lower fluence has demonstrated the feasibility on a large virus of ~1 μm.[41] Our cryo-EM results confirmed that the native influenza virus of our preparation has the size as reported [Fig. 5(f)]. The cryo-EM picture also reveals that the shape of influenza is irregular[42]—it varies from spherical, oval, and kidney shape.

To evaluate the feasibility, we first used an atomic model of the virus like particle (VLP) of Rift Valley fever virus[43] (RVFV) to conduct simulation because the size of RVFV is similar to the influenza, while the atomic model of influenza virus is not available. It is important to notice that an influenza virus is a stronger scatterer than the VLP of RVFV that has only the capsid. Compared to the VLP of RVFV that is empty inside, an influenza virus has a genome inside. Spatially, an influenza virus is a two-component system–it has a coat of 10 nm thickness and a compact core of 80 nm encapsulated by the coat [Fig. 5(f)]. The core is composed of ~14 000 RNA nucleotides organized on highly packed NP proteins, much more electron-dense than the coat, as revealed by a

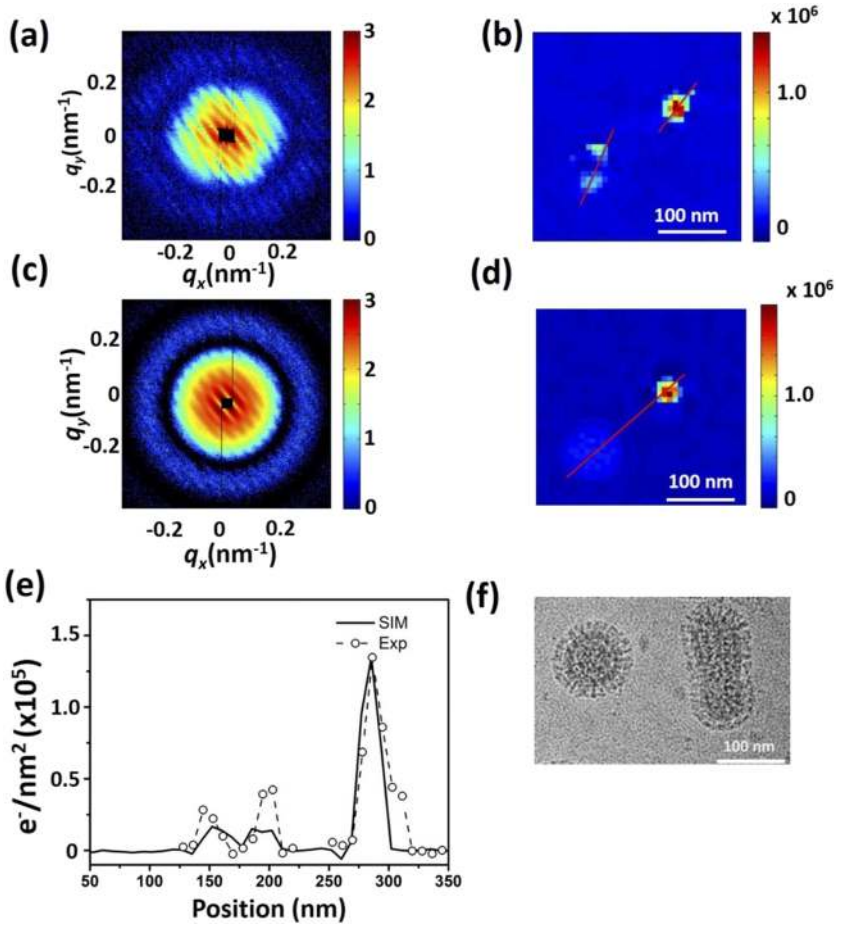

FIG. 5. AuNP–virus interference. (a) An experimental pattern of a strong scatter (40 nm AuNP) with a weak scatter of influenza virus. Note that the central region is missing. (b) The reconstructed image of (a). (c) A simulated pattern of a strong scatter (40 nm AuNP) with a weak scatter of VLP of Rift Valley fever virus. (d) The reconstructed image of (c). (e) The electron density profiles of experimental (◯) and simulated (—) images along the red line in (b) and that in (d), respectively. (f) A cryo-EM image of influenza virus from the same batch of sample. Two virus particles exhibit spherical and elongated shapes. The scale of the color bar is logarithmic in the diffraction pattern and linear in the reconstructed image (a.u.).

cryo-EM image [Fig. 5(f)]. This RNA core is estimated to contain approximately 3.5 × 10^6 electrons,[44] while the associated proteins contain 8 × 10^7 electrons. Due to the solvent effect,[37] the overall number of effective electrons of the associated proteins will be reduced[35,36] to approximately 2 × 10^7, while that of RNA is much less reduced.[45,46] Since this figure is close to but greater than that of the 20 nm AuNP, it implies that an influenza virus in water should still be detectable with the help of an enhancement technique.

The simulation on the VLP of RVFV began with a scenario without taking water into account. The RVFV VLP is an icosahedral particle (T = 12)[43] that uses a heterodimer as a building unit, where each monomer has a molecular weight of 78 kDa. By using these parameters and the estimated electron density of protein (Table I), the total number of electrons of a RVFV capsid is estimated to be ~6 × 10^7, as shown in Fig. 3 (green dot). Since this figure is between that of 20 nm and 40 nm AuNP, it is logical to expect that it can be detected by an enhancement technique in simulation. Indeed, this expectation is corroborated by the simulation results of clear interference stripes [Fig. 5(c)] from an RVFV capsid and a 40 nm Au and the resultant reconstructed image [Fig. 5(d)]. Notably, the reconstructed density of RVFV capsid amounts to a total of 1.3 × 10^7 electrons, approximately half of that anticipated from an AuNP that has similar number of total electrons. This result suggests that RVFV would be undetectable when water is present.

To appropriately handle the influenza that are infectious, we again exploited the hydrated enclosure for the XFEL imaging experiment as we did for the AuNP. Although we were able to obtain experimental speckle patterns from the bare influenza virus, the image reconstruction failed to converge. We employed the 40 nm AuNP as a reference scatterer for the influenza virus. We were able to record the CXDI pattern from a sample containing influenza viruses mixed with 40 nm AuNPs. Notably, in the interference pattern, there are stripes of two different directions [Fig. 5(a)], suggesting that there were two isolated objects. The image reconstruction did not reveal the anticipated shape of influenza due largely to the lack of resolution. Interestingly, two bright blobs were revealed [Fig. 5(b)]. The protein coat of influenza does not appear and this seems to be consistent with the expectation from the RVFV capsid in water.

What then could be the identity of those blobs? First, an individual blob spans approximately 50 nm in the electron density profile that it can be accommodated in the core of influenza. Second, the integrated number of electrons in each blob is estimated to be ~1 × 10^7, in striking agreement with what is anticipated from the

TABLE I. Electron densities, total number of electrons, and particle detectability in water with the current XFEL fluence.

Particle	Electron densities (e^-/nm^3)	Total number of electrons	Diffraction	Image reconstruction (by phase retrieval)
60 nm Au	4300	4.9×10^8	Yes	Yes
40 nm Au	4300	1.4×10^8	Yes	Yes
20 nm Au	4300	1.8×10^7	Yes (poor SNR)	Unsuccessful
20 nm Au	4300	1.8×10^7	Yes (with a 40 nm Au)	Yes
10 nm Au	4300	2.2×10^6	No	NA
100 nm RVFV (coat, simul.)	~330 (protein only)	~6.0×10^7 (coat proteins)	Yes (simulation with a 40 nm Au)	Yes but close to background
100 nm Flu (expt.)	>330	>1.0×10^8	Yes	Unsuccessful
100 nm Flu (expt.)	>330	>1.0×10^8	Yes (with a 40 nm Au)	Yes
Protein coat of Flu (expt.)	~330 (protein only)	~4×10^7	NA	
Protein core of Flu (expt.)	~330 (protein only)	~8×10^7	NA	
RNA core Flu (expt.)	>450 (from ribosome RNA)[44]	~3.5×10^6	NA	

core materials. Given that both the size and the contained electrons match well with those of the core of the influenza, we tentatively designate those blobs to be the core of influenza virus. The difficulty to examine the same "diffract-and-destroyed" sample after the XFEL measurements makes the identification of the influenza virus nearly impossible and warrants further investigations, perhaps with better statistics. Nonetheless, whatever those blobs are, their density does not allow them to be detected with our current XFEL without heterodyne enhancement.

VIII. CONCLUSION AND DISCUSSION

A central mission of the developing XFEL is to realize the structural determination of biological objects as a single particle without the need of crystal. The work on Mimivirus,[41] a virus of extraordinary size, had heralded a bright future when XFEL would be used for imaging biological macromolecules of regular size with much higher resolution. When the electron density map of a biological macromolecule reaches near atomic resolution, the identity of the object becomes self-evident. Recently, this possibility has been made available, however, not by XFEL but its competing technique of cryo-EM.[47] The success of cryo-EM is largely built upon the nature of electron—a high energy electron can give rise to a much greater number of scattering events. In fact, a high energy electron is equivalent to 10^4–10^5 x-ray photons. Since radiation damage with XFEL can be circumvented by the strategy of "diffraction before destroyed" while that with cryo-EM is by constraining the dose, it is perceived that high-resolution structural biology with XFEL single particle imaging will be realized with the ultimate increase of the fluence that yields a sufficient number of scattered photons in the high q region. Nonetheless, a road map with a quantitative framework had been lacking until this work. In this report, we employ a quantitative approach to explore the single particle detection limit of an XFEL by using AuNP particles with sizes ranging from 80 nm to 10 nm as benchmark scatterers. Specifically, we set up a detection criterion based on "identification" using the total number of effective electrons determined from the diffraction patterns. We found that the particles of 60 nm reported total electron densities close to that expected from gold atoms arranged in an fcc structure. Such agreement with gas phase data indicates that a water column of 2 μm has virtually little effect. When the particle size was reduced to 20 nm, the phase retrieval became unreliable, suggesting that it represents the detection limit of the XFEL beamline at SACLA. We also found that the phase retrieval was feasible with twin particles of 20 nm. The scattering intensity recovered at zero momentum transfer further permits SAXS analysis, by which a master curve that describes the total number of effective electrons with respect to the size of AuNPs is established whereas the measured master curve deviated slightly from the ideal one. The master curve in its normalized form has universal significance since it is a function that only depends on the size and scattering property of the particle, but not on instrumentation parameters. However, where the curve vanishes does depend on instrumentation parameters including photon fluence, and this point defines the detection limit at an XFEL. This limit can be largely eliminated, for example, by employing a high-fluence XFEL beam of 10^6 J/cm^2 and focusing it to a sub-micron spot at a new LCLS beamline[48] or other new XFELs (see Fig. 6).

Although the usage of the master curve can be straightforward, we found that a naïve application of this curve established based on AuNPs to biological objects was faced with challenges. Based on the master curve, one would expect a 100 nm virus containing genome is detectable as a single particle since the total number of electrons is greater than that of the 20 nm AuNP. Unfortunately, it is not the case in reality—image reconstruction from the diffraction patterns of influenza failed to converge. We explained this deficit by considering the effective scattering of protein in the presence of water medium. The severity of this solvent-mediated contrast effect, though well known in the Bio-SAXS community,[36,46] is perhaps disregarded by XFEL practitioners focusing on gas phase studies. This issue of water is ubiquitous as long as the protein is wet—it is regardless of whether the object is carried using a jet[41] or confined in an enclosure.[9] With the inclusion of the medium effect on a scatter, the application of the master curve can be extended to biological materials.

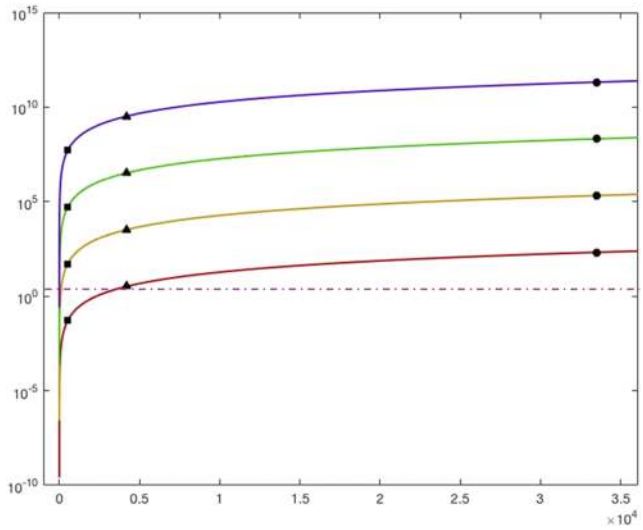

FIG. 6. A family of ideal master curves under various fluences at the sample: Red solid line, 10^{12} photons/μm^2; orange solid line, 10^{15} photons/μm^2; green solid line, 10^{18} photons/μm^2; and purple solid line, 10^{21} photons/μm^2. The unit of intensity is counts/pixel and that of size is nm^3. The curves are calculated using Eqs. (1) and (5). The scattering intensities at zero momentum transfer from different sizes of AuNP particles of spherical shape assuming the electron density of Au to be 4600 e^-/nm^3 as in an fcc structure. ● 40 nm AuNP, ▲ 20 nm AuNP, and ■ 10 nm AuNP. The scale is logarithmic in the y axis and linear in the x axis (in unit of nm^3). The pink dashed-dotted line denotes the level calculated using 20 nm AuNPs, which is the threshold of counts that allows for identification at 10^{12} photons/μm^2. The numerical values of this level are less than 30.

At the SACLA beamline used in this study, ~10^{12} photons were focused to a spot of 1.5 μm (FWHM) that the photons impinging on a 20 nm Au are approximately ~10^8. Despite that Au is a strong scatterer, the diffraction pattern is photon-limited—in the central region there are less than 30 photons per pixel and the counts progressively decrease to a noise level at a high q such that the phase retrieval would hardly converge, hampering the identification of the material through the determination of the total number of electrons. This finding is consistent with a recent gas phase study on Xe nanoparticles.[49] Currently, diffractions of many nanoscale materials can be obtained by XFEL, but the identification usually relies on correlated electron microscopy imaging.[50,51]

As a provisional remedy for imaging weak scatterers with the limiting XFEL fluence, we systematically analyzed the heterodyne enhancement effect from two-particle interference in CXDI imaging. This enhancement method, when applied to an influenza virus with a 40 nm AuNP nearby, appeared to reveal the plausible content of the virus. This work demonstrates that interference enhancement is powerful in detecting a weakly scattering biological object that is otherwise impossible. The conceptual framework of a two-particle experiment with coherent x ray for biological application was raised by Shintake,[16] but it has been limited to characterizing the transverse coherence of the XFEL beam.[52] In Shintake's proposal, the enhancing AuNP is posed proximal to a biological molecule with a linker of controllable length. We have attempted this approach by using the AuNP functionalized with streptavidin (SA) protein, but unfortunately ended up obtaining CXD patterns from aggregated particles due to the fact that there are multiple streptavidin (SA) molecules on an AuNP, whereas SA itself is also multi-valent.

In conclusion, our work establishes a framework for the quantitative understanding of the role of x-ray fluence in the single particle detection and provides the first experimental demonstration of the heterodyne effect in enhancing a weakly scatter of biological particle such as a small virus with a fluence-limited XFEL. The usage of the AuNP as a strong reference scatterer is simple and versatile for a variety of native biological assemblies.

ACKNOWLEDGMENTS

We thank Yi-Yun Chen for cryo-EM imaging in Fig. 5 and Hsin-Hung Lin for Fig. 6, and Chien-Chun Chen, Tsu-Chien Weng, and Soichi Wakatsuki for stimulating discussions. We also thank the operation and engineering staff of SACLA for assisting the XFEL experiments. This work was supported by the Ministry of Science and Technology (MOST, Taiwan) (Grant Nos. 104-2321-B-001-019 and 105-2321-B-001-009 to W.-H.C.; Nos. 104-0210-01-09-02, 105-0210-01-13-01, 106-0210-01-15-02, and 107-0210-01-19-01 to C.-H.W.), the Japan Society for the Promotion of Science KAKENHI (JSPS KAKENHI) (Grant Nos. 15H05737, 16H05989, 16K05527, and 17H04819), the X-ray Free Electron Laser Priority Strategy Program from MEXT; and the Research Program of "Five-star Alliance" and the Cooperative Research Program of "NJRC Materials and Devices," and the Japan Synchrotron Radiation Research Institute (JASRI) (Proposal Nos. 2017A8006, 2016B8065, 2016A8049, 2015B8050, 2015A8052, and 2014B8053).

REFERENCES

[1] P. Emma, R. Akre, J. Arthur, R. Bionta, C. Bostedt, J. Bozek, A. Brachmann, P. Bucksbaum, R. Coffee, F.-J. Decker, Y. Ding, D. Dowell, S. Edstrom, A. Fisher, J. Frisch, S. Gilevich, J. Hastings, G. Hays, P. Hering, Z. Huang, R. Iverson, H. Loos, M. Messerschmidt, A. Miahnahri, S. Moeller, H.-D. Nuhn, G. Pile, D. Ratner, J. Rzepiela, D. Schultz, T. Smith, P. Stefan, H. Tompkins, J. Turner, J. Welch, W. White, J. Wu, G. Yocky, and J. Galayda, "First lasing and operation of an ångstrom-wavelength free-electron laser," Nat. Photonics **4**, 641 (2010).

[2] T. Ishikawa, H. Aoyagi, T. Asaka, Y. Asano, N. Azumi, T. Bizen, H. Ego, K. Fukami, T. Fukui, Y. Furukawa, S. Goto, H. Hanaki, T. Hara, T. Hasegawa, T. Hatsui, A. Higashiya, T. Hirono, N. Hosoda, M. Ishii, T. Inagaki, Y. Inubushi, T. Itoga, Y. Joti, M. Kago, T. Kameshima, H. Kimura, Y. Kirihara, A. Kiyomichi, T. Kobayashi, C. Kondo, T. Kudo, H. Maesaka, X. M. Maréchal, T. Masuda, S. Matsubara, T. Matsumoto, T. Matsushita, S. Matsui, M. Nagasono, N. Nariyama, H. Ohashi, T. Ohata, T. Ohshima, S. Ono, Y. Otake, C. Saji, T. Sakurai, T. Sato, K. Sawada, T. Seike, K. Shirasawa, T. Sugimoto, S. Suzuki, S. Takahashi, H. Takebe, K. Takeshita, K. Tamasaku, H. Tanaka, R. Tanaka, T. Tanaka, T. Togashi, K. Togawa, A. Tokuhisa, H. Tomizawa, K. Tono, S. Wu, M. Yabashi, M. Yamaga, A. Yamashita, K. Yanagida, C. Zhang, T. Shintake, H. Kitamura, and N. Kumagai, "A compact X-ray free-electron laser emitting in the sub-ångström region," Nat. Photonics **6**, 540 (2012).

[3] J. Miao, P. Charalambous, J. Kirz, and D. Sayre, "Extending the methodology of X-ray crystallography to allow imaging of micrometre-sized non-crystalline specimens," Nature **400**, 342 (1999).

[4] J. Miao, T. Ishikawa, Q. Shen, and T. Earnest, "Extending X-ray crystallography to allow the imaging of noncrystalline materials, cells and single protein complexes," Annu. Rev. Phys. Chem. **59**, 387–410 (2008).

[5] J. Miao, J. E. Amonette, Y. Nishino, T. Ishikawa, and K. O. Hodgson, "Direct determination of the absolute electron density of nanostructured and disordered materials at sub-10-nm resolution," Phys. Rev. B **68**, 012201 (2003).

[6]H. N. Chapman, A. Barty, M. J. Bogan, S. Boutet, M. Frank, S. P. Hau-Riege, S. Marchesini, B. W. Woods, S. Bajt, W. H. Benner, R. A. London, E. Plönjes, M. Kuhlmann, R. Treusch, S. Düsterer, T. Tschentscher, J. R. Schneider, E. Spiller, T. Möller, C. Bostedt, M. Hoener, D. A. Shapiro, K. O. Hodgson, D. van der Spoel, F. Burmeister, M. Bergh, C. Caleman, G. Huldt, M. M. Seibert, F. R. N. C. Maia, R. W. Lee, A. Szöke, N. Timneanu, and J. Hajdu, "Femtosecond diffractive imaging with a soft-X-ray free-electron laser," Nat. Phys. **2**, 839 (2006).

[7]R. Neutze, R. Wouts, D. van der Spoel, E. Weckert, and J. Hajdu, "Potential for biomolecular imaging with femtosecond X-ray pulses," Nature **406**, 752 (2000).

[8]J. C. Spence and R. B. Doak, "Single molecule diffraction," Phys. Rev. Lett. **92**, 198102 (2004).

[9]T. Kimura, Y. Joti, A. Shibuya, C. Song, S. Kim, K. Tono, M. Yabashi, M. Tamakoshi, T. Moriya, T. Oshima, T. Ishikawa, Y. Bessho, and Y. Nishino, "Imaging live cell in micro-liquid enclosure by X-ray laser diffraction," Nat. Commun. **5**, 3052 (2014).

[10]R. Yoshida, H. Yamashige, M. Miura, T. Kimura, Y. Joti, Y. Bessho, M. Kuramoto, J. Yu, K. Khakurel, K. Tono, M. Yabashi, T. Ishikawa, and Y. Nishino, "Extending the potential of x-ray free-electron lasers to industrial applications—An initiatory attempt at coherent diffractive imaging on car-related nanomaterials," J. Phys. B: At., Mol. Opt. Phys. **48**, 244008 (2015).

[11]K. Ayyer, A. J. Morgan, A. Aquila, H. Demirci, B. G. Hogue, R. A. Kirian, P. L. Xavier, C. H. Yoon, H. N. Chapman, and A. Barty, "Low-signal limit of X-ray single particle diffractive imaging," Opt. Express **27**, 37816 (2019).

[12]J. Miao, T. Ishikawa, I. K. Robinson, and M. M. Murnane, "Beyond crystallography: Diffractive imaging using coherent x-ray light sources," Science **348**, 530–535 (2015).

[13]T.-Y. Lan, P.-N. Li, and T.-K. Lee, "Method to enhance the resolution of x-ray coherent diffraction imaging for non-crystalline bio-samples," New J. Phys. **16**, 033016 (2014).

[14]A. V. Martin, N. D. Loh, C. Y. Hampton, R. G. Sierra, F. Wang, A. Aquila, S. Bajt, M. Barthelmess, C. Bostedt, J. D. Bozek, N. Coppola, S. W. Epp, B. Erk, H. Fleckenstein, L. Foucar, M. Frank, H. Graafsma, L. Gumprecht, A. Hartmann, R. Hartmann, G. Hauser, H. Hirsemann, P. Holl, S. Kassemeyer, N. Kimmel, M. Liang, L. Lomb, F. R. N. C. Maia, S. Marchesini, K. Nass, E. Pedersoli, C. Reich, D. Rolles, B. Rudek, A. Rudenko, J. Schulz, R. L. Shoeman, H. Soltau, D. Starodub, J. Steinbrener, F. Stellato, L. Strüder, J. Ullrich, G. Weidenspointner, T. A. White, C. B. Wunderer, A. Barty, I. Schlichting, M. J. Bogan, and H. N. Chapman, "Femtosecond dark-field imaging with an X-ray free electron laser," Opt. Express **20**, 13501–13512 (2012).

[15]S. Marchesini, S. Boutet, A. E. Sakdinawat, M. J. Bogan, S. Bajt, A. Barty, H. N. Chapman, M. Frank, S. P. Hau-Riege, A. Szöke, C. Cui, D. A. Shapiro, M. R. Howells, J. C. H. Spence, J. W. Shaevitz, J. Y. Lee, J. Hajdu, and M. M. Seibert, "Massively parallel X-ray holography," Nat. Photonics **2**, 560 (2008).

[16]T. Shintake, "Possibility of single biomolecule imaging with coherent amplification of weak scattering x-ray photons," Phys. Rev. E **78**, 041906 (2008).

[17]C. Kim, Y. Kim, and C. Song, "Enhancing resolution in coherent x-ray diffraction imaging," J. Phys.: Condens. Matter **28**, 493001 (2016).

[18]Y. Takayama and K. Yonekura, "Cryogenic coherent X-ray diffraction imaging of biological samples at SACLA: A correlative approach with cryo-electron and light microscopy," Acta Crystallogr., Sect. A: Found. Adv. **72**, 179–189 (2016).

[19]K. Tono, T. Togashi, Y. Inubushi, T. Sato, T. Katayama, K. Ogawa, H. Ohashi, H. Kimura, S. Takahashi, K. Takeshita, H. Tomizawa, S. Goto, T. Ishikawa, and M. Yabashi, "Beamline, experimental stations and photon beam diagnostics for the hard x-ray free electron laser of SACLA," New J. Phys. **15**, 083035 (2013).

[20]H. Yumoto, H. Mimura, T. Koyama, S. Matsuyama, K. Tono, T. Togashi, Y. Inubushi, T. Sato, T. Tanaka, T. Kimura, H. Yokoyama, J. Kim, Y. Sano, Y. Hachisu, M. Yabashi, H. Ohashi, H. Ohmori, T. Ishikawa, and K. Yamauchi, "Focusing of X-ray free-electron laser pulses with reflective optics," Nat. Photonics **7**, 43 (2013).

[21]T. Kameshima, S. Ono, T. Kudo, K. Ozaki, Y. Kirihara, K. Kobayashi, Y. Inubushi, M. Yabashi, T. Horigome, A. Holland, K. Holland, D. Burt, H. Murao, and T. Hatsui, "Development of an X-ray pixel detector with multi-port charge-coupled device for X-ray free-electron laser experiments," Rev. Sci. Instrum. **85**, 033110 (2014).

[22]A. Guinier and G. Fournet, *Small-Angle Scattering of X-Rays* (Wiley & Sons, NY, 1955).

[23]C. Song, K. Tono, J. Park, T. Ebisu, S. Kim, H. Shimada, S. Kim, M. Gallagher-Jones, D. Nam, T. Sato, T. Togashi, K. Ogawa, Y. Joti, T. Kameshima, S. Ono, T. Hatsui, S. Iwata, M. Yabashi, and T. Ishikawa, "Multiple application X-ray imaging chamber for single-shot diffraction experiments with femtosecond X-ray laser pulses," J. Appl. Crystallogr. **47**, 188–197 (2014).

[24]M. F. Hantke, D. Hasse, T. Ekeberg, K. John, M. Svenda, D. Loh, A. V. Martin, N. Timneanu, D. S. Larsson, and G. Van Der Schot, "A data set from flash X-ray imaging of carboxysomes," Sci. Data **3**, 160061 (2016).

[25]B. E. Warren, *X-ray Diffraction* (Courier Corporation, 1990).

[26]J. Fan, Z. Sun, Y. Wang, J. Park, S. Kim, M. Gallagher-Jones, Y. Kim, C. Song, S. Yao, and J. Zhang, "Single-pulse enhanced coherent diffraction imaging of bacteria with an X-ray free-electron laser," Sci. Rep. **6**, 34008 (2016).

[27]K. P. Khakurel, T. Kimura, Y. Joti, S. Matsuyama, K. Yamauchi, and Y. Nishino, "Coherent diffraction imaging of non-isolated object with apodized illumination," Opt. Express **23**, 28182–28190 (2015).

[28]D. Nam, J. Park, M. Gallagher-Jones, S. Kim, S. Kim, Y. Kohmura, H. Naitow, N. Kunishima, T. Yoshida, T. Ishikawaand, and C. Song, "Imaging fully hydrated whole cells by coherent x-ray diffraction microscopy," Phys. Rev. Lett. **110**, 098103 (2013).

[29]M. Nakano, O. Miyashita, S. Jonic, C. Song, D. Nam, Y. Joti, and F. Tama, "Three-dimensional reconstruction for coherent diffraction patterns obtained by XFEL," J. Synchrotron Radiat. **24**, 727–737 (2017).

[30]R. Xu, S. Salha, K. S. Raines, H. Jiang, C.-C. Chen, Y. Takahashi, Y. Kohmura, Y. Nishino, C. Song, T. Ishikawa, and J. Miao, "Coherent diffraction microscopy at SPring-8: Instrumentation, data acquisition and data analysis," J. Synchrotron Radiat. **18**, 293–298 (2011).

[31]C.-C. Chen, J. Miao, C. W. Wang, and T. K. Lee, "Application of optimization technique to noncrystalline x-ray diffraction microscopy: Guided hybrid input-output method," Phys. Rev. B **76**, 064113 (2007).

[32]S. Marchesini, H. He, H. N. Chapman, S. P. Hau-Riege, A. Noy, M. R. Howells, U. Weierstall, and J. C. Spence, "X-ray image reconstruction from a diffraction pattern alone," Phys. Rev. B **68**, 140101 (2003).

[33]M. Kotlarchyk and S. H. Chen, "Analysis of small angle neutron scattering spectra from polydisperse interacting colloids," J. Chem. Phys. **79**, 2461–2469 (1983).

[34]B. Hammouda and D. F. R. Mildner, "Small-angle neutron scattering resolution with refractive optics," J. Appl. Crystallogr. **40**, 250–259 (2007).

[35]E. Mylonas and D. I. Svergun, "Accuracy of molecular mass determination of proteins in solution by small-angle X-ray scattering," J. Appl. Crystallogr. **40**, s245–s249 (2007).

[36]S. Doniach and J. Lipfert, "Small and wide angle X-ray scattering from biological macromolecules and their complexes in solution ," Compr. Biophys. **1**, 376–397 (2012).

[37]Z. Sun, J. Fan, H. Li, and H. Jiang, "Current status of single particle imaging with X-ray lasers," Appl. Sci. **8**, 132 (2018).

[38]Y. Takayama, S. Maki-Yonekura, T. Oroguchi, M. Nakasako, and K. Yonekura, "Signal enhancement and Patterson-search phasing for high-spatial-resolution coherent X-ray diffraction imaging of biological objects," Sci. Rep. **5**, 8074 (2015).

[39]T. Gorkhover, A. Ulmer, K. Ferguson, M. Bucher, F. R. N. C. Maia, J. Bielecki, T. Ekeberg, M. F. Hantke, B. J. Daurer, C. Nettelblad, J. Andreasson, A. Barty, P. Bruza, S. Carron, D. Hasse, J. Krzywinski, D. S. D. Larsson, A. Morgan, K. Mühlig, M. Müller, K. Okamoto, A. Pietrini, D. Rupp, M. Sauppe, G. van der Schot, M. Seibert, J. A. Sellberg, M. Svenda, M. Swiggers, N. Timneanu, D. Westphal, G. Williams, A. Zani, H. N. Chapman, G. Faigel, T. Möller, J. Hajdu, and C. Bostedt, "Femtosecond X-ray Fourier holography imaging of free-flying nanoparticles," Nat. Photonics **12**, 150 (2018).

[40]A. Harris, G. Cardone, D. C. Winkler, J. B. Heymann, M. Brecher, J. M. White, and A. C. Steven, "Influenza virus pleiomorphy characterized by cryoelectron tomography," Proc. Natl. Acad. Sci. U. S. A. **103**, 19123–19127 (2006).

[41]M. M. Seibert *et al.*, "Single mimivirus particles intercepted and imaged with an X-ray laser," Nature **470**, 78–81 (2011).

[42]R. W. H. Ruigrok, P. J. Andree, R. A. M. Hooft Van Huysduynen, and J. E. Mellema, "Characterization of three highly purified influenza virus strains by electron microscopy," J. Gen. Virol. **65**, 799–802 (1984).
[43]M. B. Sherman, A. N. Freiberg, M. R. Holbrook, and S. J. Watowich, "Single-particle cryo-electron microscopy of Rift Valley fever virus," Virology **387**, 11–15 (2009).
[44]D. I. Svergun, M. H. J. Koch, and I. N. Serdyuk, "Structural model of the 50 S subunit of *Escherichia coli* ribosomes from solution scattering: I. X-ray synchroton radiation study," J. Mol. Biol. **240**, 66–77 (1994).
[45]Y. Chen, J. M. Tokuda, T. Topping, J. L. Sutton, S. P. Meisburger, S. A. Pabit, L. M. Gloss, and L. Pollack, "Revealing transient structures of nucleosomes as DNA unwinds," Nucleic Acids Res. **42**, 8767–8776 (2014).
[46]Y. Chen and L. Pollack, "SAXS studies of RNA: Structures, dynamics, and interactions with partners," Wiley Interdiscip. Rev.: RNA **7**, 512–526 (2016).
[47]D. Cressey and E. Callaway, "Cryo-electron microscopy wins chemistry Nobel," Nature **550**, 167 (2017).
[48]K. R. Beyerlein *et al.*, "Ultrafast nonthermal heating of water initiated by an X-ray free-flectron laser," Proc. Natl. Acad. Sci. U. S. A. **115**, 5652–5657 (2018).
[49]T. Nishiyama, A. Niozu *et al.*, "Refinement for single-nanoparticle structure determination from low-quality single-shot coherent diffraction data," IUCrJ **7**, 10–17 (2020).
[50]C.-F. Huang, K. S. Liang, T.-L. Hsu, T.-T. Lee, Y.-Y. Chen, S.-M. Yang, H.-H. Chen, S.-H. Huang, W.-H. Chang, T.-K. Lee, P. Chen, K.-E. Peng, C.-C. Chen, C.-Z. Shi, Y.-F. Hu, G. Margaritondo, T. Ishikawa, C.-H. Wong, and Y. Hwu, "Free-electron-laser coherent diffraction images of individual drug-carrying liposome particles in solution," Nanoscale **10**, 2820–2824 (2018).
[51]X. Li *et al.*, "Diffraction data of core-shell nanoparticles from an X-ray free electron laser," Sci. Data **4**, 170048 (2017).
[52]I. Inoue, K. Tono, Y. Joti, T. Kameshima, K. Ogawa, Y. Shinohara, Y. Amemiya, and M. Yabashi, "Characterizing transverse coherence of an ultra-intense focused X-ray free-electron laser by an extended Young's experiment," IUCrJ **2**, 620–626 (2015).